

RESEARCH ARTICLE | APRIL 03 2024

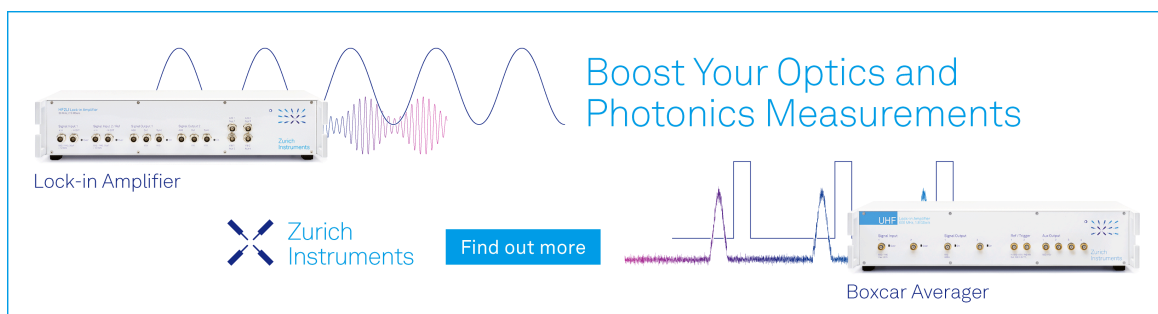
Modulation of supramolecular structure by stepwise removal of *tert*-butyl groups from tetraazaperopyrene derivatives on Ag(111) **FREE**

Boyu Fu ; Yurou Guan; Wei Yuan; Jianqun Geng ; Zhenliang Hao; Zilin Ruan; Shijie Sun ;
Yong Zhang ; Wei Xiong; Lei Gao  ; Yulan Chen  ; Wei Ji  ; Jianchen Lu  ;
Jinming Cai  



J. Chem. Phys. 160, 134308 (2024)

<https://doi.org/10.1063/5.0196443>



Boost Your Optics and
Photonics Measurements

Lock-in Amplifier

Zurich
Instruments

Find out more

Boxcar Averager

Modulation of supramolecular structure by stepwise removal of *tert*-butyl groups from tetraazaperopyrene derivatives on Ag(111)

Cite as: J. Chem. Phys. 160, 134308 (2024); doi: 10.1063/5.0196443

Submitted: 7 January 2024 • Accepted: 4 March 2024 •

Published Online: 3 April 2024



View Online



Export Citation



CrossMark

Boyu Fu,¹ Yurou Guan,^{2,3} Wei Yuan,⁴ Jianqun Geng,¹ Zhenliang Hao,¹ Zilin Ruan,¹ Shijie Sun,¹ Yong Zhang,¹ Wei Xiong,¹ Lei Gao,^{5,a)} Yulan Chen,^{4,a)} Wei Ji,^{2,3,a)} Jianchen Lu,^{1,a)} and Jinming Cai^{1,a)}

AFFILIATIONS

¹ Faculty of Materials Science and Engineering, Kunming University of Science and Technology, No. 68 Wenchang Road, Kunming 650093, China

² Beijing Key Laboratory of Optoelectronic Functional Materials & Micro-Nano Devices, Department of Physics, Renmin University of China, Beijing 100872, People's Republic of China

³ Key Laboratory of Quantum State Construction and Manipulation (Ministry of Education), Renmin University of China, Beijing 100872, China

⁴ College of Chemistry, Jilin University, No. 2699 Qianjin Street, Jilin 130012, China

⁵ Faculty of Science, Kunming University of Science and Technology, No. 727 Jingming South Road, Kunming 650500, China

^{a)} Authors to whom correspondence should be addressed: lgao@kust.edu.cn; yulanchen@jlu.edu.cn; wji@ruc.edu.cn; jclu@kust.edu.cn; and j.cai@kust.edu.cn

ABSTRACT

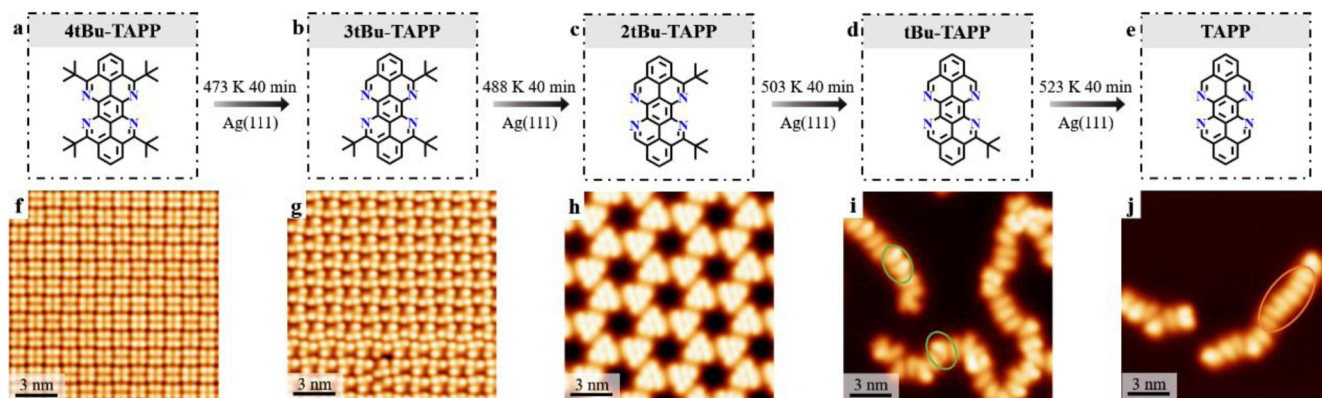
Tert-butyl functional groups can modulate the self-assembly behavior of organic molecules on surfaces. However, the precise construction of supramolecular architectures through their controlled thermal removal remains a challenge. Herein, we precisely controlled the removal amount of *tert*-butyl groups in tetraazaperopyrene derivatives by stepwise annealing on Ag(111). The evolution of 4tBu-TAPP supramolecular self-assembly from the grid-like structure composed of 3tBu-TAPP through the honeycomb network formed by 2tBu-TAPP to the one-dimensional chain co-assembled by tBu-TAPP and TAPP was successfully realized. This series of supramolecular nanostructures were directly visualized by high resolution scanning tunneling microscopy. Tip manipulation and density functional theory calculations show that the formation of honeycomb network structure can be attributed to the van der Waals interactions, N–Ag–N coordination bonds, and weak C–H···N hydrogen bonds. Further addition of two *tert*-butyl groups (6tBu-TAPP) leads to a completely different assembly evolution, due to the fact that the additional *tert*-butyl groups affect the molecular adsorption behavior and ultimately induce desorption. This work can possibly be exploited in constructing stable and long-range ordered nanostructures in surface-assisted systems, which can also promote the development of nanostructures in functional molecular devices.

Published under an exclusive license by AIP Publishing. <https://doi.org/10.1063/5.0196443>

INTRODUCTION

Fabrication of ordered supramolecular nanostructures at the molecular level by the “bottom-up” method has attracted much attention because of its potential applications in biochemical sensing, chiral catalysis, organic functional molecular devices, etc.^{1–6}

Specific functional groups can strongly affect the adsorption and self-ordering properties of supramolecular nanostructures.⁷ To date, there have been many studies involved in the use of functional groups with different properties to modify organic molecules, thereby promoting the synthesis of diverse nanostructures.^{8–13} The *tert*-butyl group, as an effective protecting and blocking group,



SCHEME 1. Structural transformation of 4tBu-TAPP on Ag(111) via stepwise thermal removal of *tert*-butyl groups. (a)–(e) A series of product structures during *tert*-butyl thermal removal. (f) Self-assembled STM image of 4tBu-TAPP deposited on Ag(111) hold at 300 K. (g) STM image of grid-like structures formed by 3tBu-TAPP after annealing at 473 K for 40 min. (h) STM image of honeycomb networks formed by 2tBu-TAPP after annealing at 488 K for 40 min. STM images of chain structures formed by tBu-TAPP (marked by green circles) after annealing at 503 K for 40 min (i) or TAPP (marked by an orange circle) after annealing at 523 K for 40 min (j). Tunneling parameters: (f) $U = -0.60$ V, $I = 0.05$ nA; (g) $U = -0.20$ V, $I = 0.05$ nA; (h) $U = -0.60$ V, $I = 0.26$ nA; (i) and (j) $U = 0.70$ V, $I = 0.06$ nA.

is often employed in the field of synthetic organic chemistry.^{14,15} It has been found that due to enhanced intermolecular interactions, the *tert*-butyl group can regulate the diffusion behavior of organic molecules on the surface and change the self-assembly properties of organic molecules.^{16–18} In addition, *tert*-butyl is usually used to assist in monitoring the molecular rotation process due to its bright characteristics in scanning tunneling microscopy (STM) characterization.¹⁹

Controllable removal of functional groups can be achieved through several methods, such as tip manipulation, localized surface plasmon,²⁰ and thermal annealing. The first two methods utilize electron injection and light excitation to obtain reactivity inaccessible to conventional solution chemistry and thermodynamically unfavorable surface reactions, respectively. However, due to their control difficulties, these two methods are mostly used in single-molecule chemistry. For comparison, thermal annealing can efficiently obtain mass production of functional group removal products. The space-time observations of this thermal removal process and its effects on the surface assembly structure have not been explored.

Here, we report the stepwise thermal removal of *tert*-butyl groups using 3,6,10,13-tetra-*tert*-butyl-4,5,11,12-tetraazaperopyrenes (4tBu-TAPP) as a typical precursor on Ag(111) (Scheme 1). According to the number of *tert*-butyl groups in the precursor, the as-formed products obtained by gradient annealing were successively named as 3tBu-TAPP [Scheme 1(b)], 2tBu-TAPP [Scheme 1(c)], tBu-TAPP [Scheme 1(d)], and TAPP [Scheme 1(e)]. A series of supramolecular nanostructures constructed by the above products have been characterized in detail by scanning tunneling microscopy (STM), including a regular 4tBu-TAPP self-assembly structure [Scheme 1(f)], a grid-like structure [Scheme 1(g)], a honeycomb network [Scheme 1(h)], and a chain structure [Schemes 1(i) and 1(j)]. Tip manipulation and density functional theory (DFT) calculations reveal the formation mechanism of honeycomb assembly structures (N–Ag–N coordination bonds and

van der Waals interactions). A stepwise annealing experiment of 1,3,6,8,10,13-hexa-*tert*-butyl-4,5,11,12-tetraazaperopyrenes (6tBu-TAPP) on Ag(111) supplemented that terminal *tert*-butyl groups require a higher removal temperature, which would affect the adsorption behavior and weaken the modulation of the assembled structure by the surface atoms. (See Fig. S1 for the synthesis details of 4tBu-TAPP and 6tBu-TAPP.)

RESULTS AND DISCUSSION

The deposition of 4tBu-TAPP onto the Ag(111) surface held at room temperature (RT) resulted in the formation of a large-scale close-packed self-assembly structure [Fig. 1(a)]. According to previous studies,^{16,17,21} *tert*-butyl groups presented bright protrusions in the STM images due to their considerable height. Thus, Fig. 1(b) shows a magnified STM image, in which the four bright protrusions circled by yellow dashed circles represent a monomer. The distance between two protrusions of two adjacent molecules is measured to be different (7.1 ± 0.5 and 6.3 ± 0.5 Å). It can be inferred that the molecules benefit from intermolecular van der Waals forces, facilitating its adsorption to the substrate in two orientations (with an angle of 90°). The DFT calculations reveal that it is more energetically favorable when adding Ag adatoms (see Fig. S2 for details). Figure 1(c) shows its specific structural model. The *tert*-butyl group possesses a high apparent height and, therefore, seriously affects our detection of Ag adatoms. The unit cell size of the optimized model ($a = 1.95$ nm, $b = 2.08$ nm, $\alpha = 90^\circ$) agrees well with the experimental values ($a = 1.90 \pm 0.05$ nm, $b = 2.03 \pm 0.05$ nm, $\alpha = 90^\circ$). We then also performed scanning tunneling spectra (dI/dV) experiments as shown in Fig. S3. Combined with DFT calculations, the DFT-calculated LDOS maps exhibit excellent agreement with the experimental constant-current dI/dV maps. The electronic states are localized in the *tert*-butyl groups, and there is even a strong aggregation of electronic states between *tert*-butyl groups of different monomers at 1.10 V.

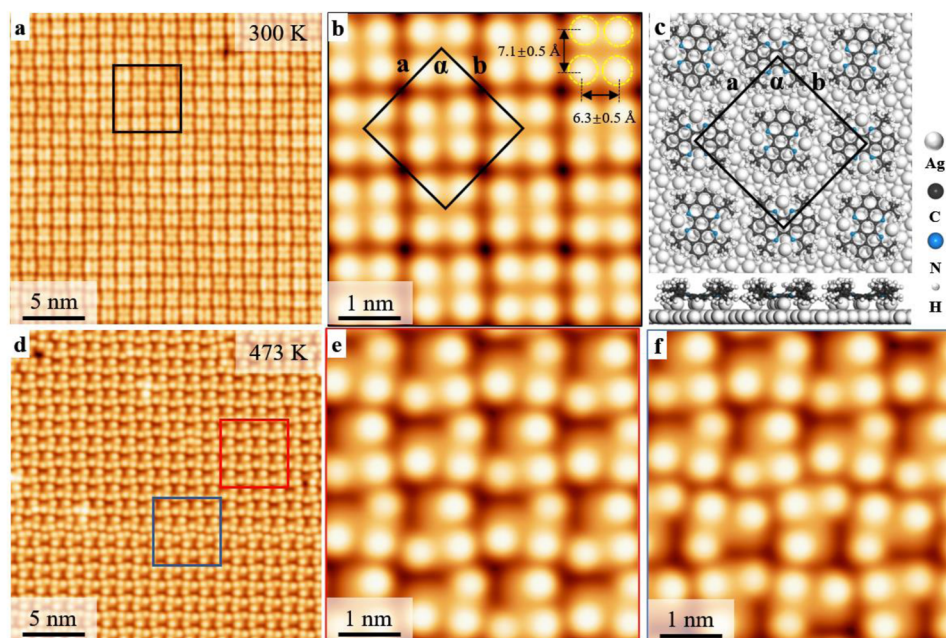


FIG. 1. Transformation from 4tBu-TAPP self-assembly to 3tBu-TAPP grid-like structures on Ag(111). (a) and (b) Large-scale and magnified STM images of 4tBu-TAPP deposited on Ag(111) kept at 300 K. A unit cell is highlighted by the rhombus in (b); *tert*-butyl groups of monomer are circled by yellow dashed lines. (c) DFT optimized structure on Ag(111). (d)–(f) Large-scale and magnified STM images marked by red and blue squares in (d) of grid-like structures on Ag(111) annealed at 473 K for 40 min. Tunneling parameters: (a) $U = 1.00$ V, $I = 0.05$ nA; (b) $U = -0.5$ V, $I = 0.08$ nA; (d) $U = -0.40$ V, $I = 0.05$ nA; (e) and (f) $U = -0.20$ V, $I = 0.12$ nA.

After annealing above sample at 473 K for 40 min, partial removal of the *tert*-butyl groups occurred and the molecules assembled into the grid-like structures as shown in Fig. 1(d). The magnified images in Figs. 1(e) and 1(f) [marked by red and blue squares in Fig. 1(d)] show that the grid-like structures are composed of L-shaped monomers containing three bright protrusions, which can be attributed to 3tBu-TAPP. It is worth noting that after the removal of one *tert*-butyl group, the intermolecular arrangement undergoes slight distortion compared to the previous self-assembly, primarily due to alterations in the van der Waals interaction between the molecules.

Subsequent thermal annealing of the sample at 488 K for about 40 min induced further *tert*-butyl removal. Figure 2(a) shows large-scale chiral honeycomb networks with a unit cell of $a = 3.885 \pm 0.05$ nm and $\gamma = 60^\circ$ (see Fig. S4 for details of its chirality). As shown in the magnified image of Fig. 2(b), a hexagonal structure is composed of six triangular units, which contains six bright protrusions. The distance between the two bright protrusions [red line in Fig. 2(c)] is measured to be 6.3 ± 0.5 Å, which agrees with the DFT-calculated distance between two *tert*-butyl groups on the same side of 4tBu-TAPP. Therefore, we confirm that each triangular unit is composed of three 2tBu-TAPP (ipsilateral removal of two *tert*-butyl groups) placed in the structural model in Fig. 2(b) by intermolecular van der Waals interactions.

We then focus on the connection mechanism between triangular units. The magnified image in the upper part of Fig. 2(c) [marked by a red dotted square in Fig. 2(b)] shows the detailed structures of the 2tBu-TAPP dimer. The alignment of the two

2tBu-TAPP at the junction suggests that contains an Ag adatom, which likely forms the N–Ag–N coordination bonds to stabilize this network. This stabilization occurs after the free radicals resulting from the removal of the *tert*-butyl group become saturated by the H atoms in the cavity. The apparent height of the *tert*-butyl group influences the observation of Ag adatoms. Therefore, the stable mode of free radicals is discussed in the subsequent section on complete removal of *tert*-butyl. Combined with DFT calculations (Fig. S5), we can prove the N–Ag–N coordination bond through the following points: (i) Fig. 2(d) shows the optimized model of Ag adatom mediated dimer with the highest stability (-3.107 eV), where the Ag adatom tends to form N–Ag–N metal coordination bonds^{22,23} with the nitrogen atoms with unpaired electrons in the molecule (Fig. S6). (ii) The theoretical value between the center of two molecules in the dimer is 1.129 nm (Table S1), which matches well with the experimental measurement of 1.12 ± 0.05 nm as shown in Fig. 2(e). (iii) Tip manipulation method is used to further demonstrate these assembly mechanisms as shown in Figs. 2(f)–2(i) and Fig. S7. Different tunneling currents of 1.8 and 2.0 nA are applied to drag the monomer along the white and green arrow directions shown in Figs. 2(f) and 2(h). Figures 2(g) and 2(i) show that the 2tBu-TAPP monomer (marked by a white circle) and the 2tBu-TAPP dimer (marked by a green circle) were successfully detached under tip manipulation, respectively. This indicates that the N–Ag–N coordination bonds in the dimer are significantly stronger than the van der Waals interactions between *tert*-butyl groups. (iv) Evidence of the N–Ag bond is also found at the end of a TAPP chain, where the *tert*-butyl location has also been passivated

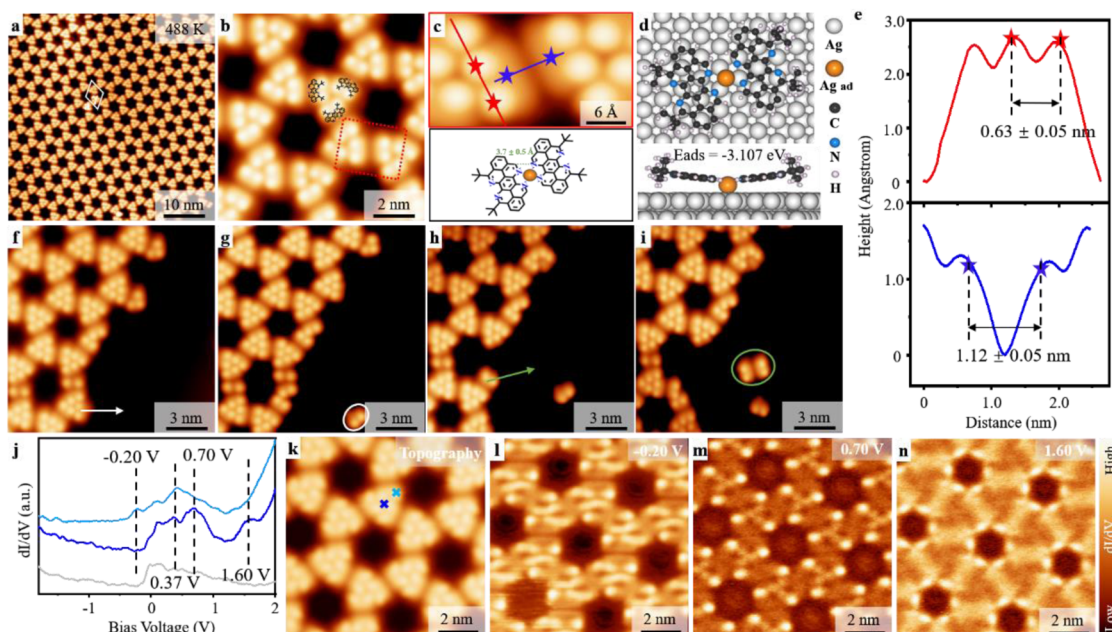


FIG. 2. Formation of 2tBu-TAPP honeycomb networks on Ag(111) after annealing at 488 K for 40 min. Large-scale (a) and close-up (b) STM images of two-dimensional honeycomb networks. A unit cell is highlighted by the white rhombus in (a). The dimer is marked by a red dotted square. (c) Magnified image of the red dotted square in (b) and corresponding molecular models. The red and blue lines indicate that the distance between two *tert*-butyl groups and the intermolecular distance of the dimer. The green dotted line indicates C–H ··· N hydrogen bonds. (d) Top and side views of DFT optimized dimers. (e) Line profiles of the red and blue lines in (c). STM images before (f) and after (g) and (i) tip manipulation. The white and green arrows indicate the direction of pulling the target structure. The white and green circles represent the structures after tip manipulation. (j) Differential conductance dI/dV spectra. The gray curve is taken on a bare Ag(111) surface. (k) STM topographic image of honeycomb networks. The blue and light blue crosses correspond to the positions of the dI/dV spectra shown in (j). (l)–(n) The corresponding dI/dV maps. Tunneling parameters: (a) $U = -0.30$ V, $I = 0.06$ nA; (b) $U = -0.30$ V, $I = 0.08$ nA; (c) $U = 0.60$ V, $I = 0.40$ nA; (f)–(i) $U = -0.40$ V, $I = 0.05$ nA; (k) $U = -0.20$ V, $I = 0.10$ nA.

by H [Figs. S9(g) and S9(h)]. In addition, the distance between the H and N atoms [green dotted line in the bottom half of Fig. 2(c)] is measured to be 3.7 ± 0.5 Å, corresponding to the bond length of a weak hydrogen bond. Consequently, N–Ag–N coordination bonds, weak hydrogen bonds, and van der Waals interactions are deemed to constitute a honeycomb network with an optimized structure of rhomboid cells, with $a = 3.90$ nm and $\gamma = 60^\circ$, as depicted in Fig. S8(b).

To investigate the electronic properties of the honeycomb networks, we performed STS measurements. The dI/dV spectra of Fig. 2(j) acquired above the center and vertices of a triangle unit [marked in Fig. 2(k)] show prominent peaks in the density of states at -0.20 , 0.37 , 0.70 , and 1.60 V. Figures 2(l) and 2(m) (-0.20 and 0.70 V) show that the *tert*-butyl substituents resolved more clearly. Inside the triangle, the electronic states can be attributed to the interaction between three molecules. On the contrary, the dI/dV mapping at 1.60 V [Fig. 2(n)] shows that the electronic states are mainly concentrated at the edge of the hole and at the connection of the triangle units. The DFT-calculated projected density of states (PDOS) maps at the partial energy positions match very well with the experimental evidence (Fig. S8), which effectively allows us to visualize the spatial distribution of these states.

In addition, the deformed hexagonal networks shown in the white dashed square of Fig. 3(a) can also be observed. Figure 3(b)

shows the deformed hexagonal structure consisting of six triangles and two to four small rectangles, where the pink dotted square marks a new trimer. The corresponding magnified image in the upper part of Fig. 3(c) shows that there is a molecule sandwiched between two 2tBu-TAPP molecules, which contains two bright protrusions (marked by green dotted circles). As shown in Fig. 3(e), the distance between these two bright protrusions [green line in Fig. 3(c)] is 1.10 ± 0.05 nm, which is different from the previously mentioned 2tBu-TAPP. This phenomenon also indicates that the adulterated component may be a novel 2tBu-TAPP (products of diagonal removal of two *tert*-butyl groups). The corresponding structure models of trimer are shown in the bottom part of Fig. 3(c). Since such deformed hexagonal structures are very rare, it is more difficult to remove the *tert*-butyl group in the diagonal way.

To explore the influence of deformed hexagonal networks on the electronic properties, we conducted STS measurements. Figure 3(d) shows differential conductance point spectra dI/dV acquired at the positions marked by the crosses in Fig. 3(b). The constant-current dI/dV mappings obtained at different biases [Figs. 3(f)–3(h)] intuitively show the difference in the dI/dV spectra for the doping section and regular network. Figures 3(f) and 3(g) show that doping parts are resolved more clearly than regular networks. The difference is that the density of electronic states at 0.79 V is densely localized on the *tert*-butyl groups of diagonal 2tBu-TAPP

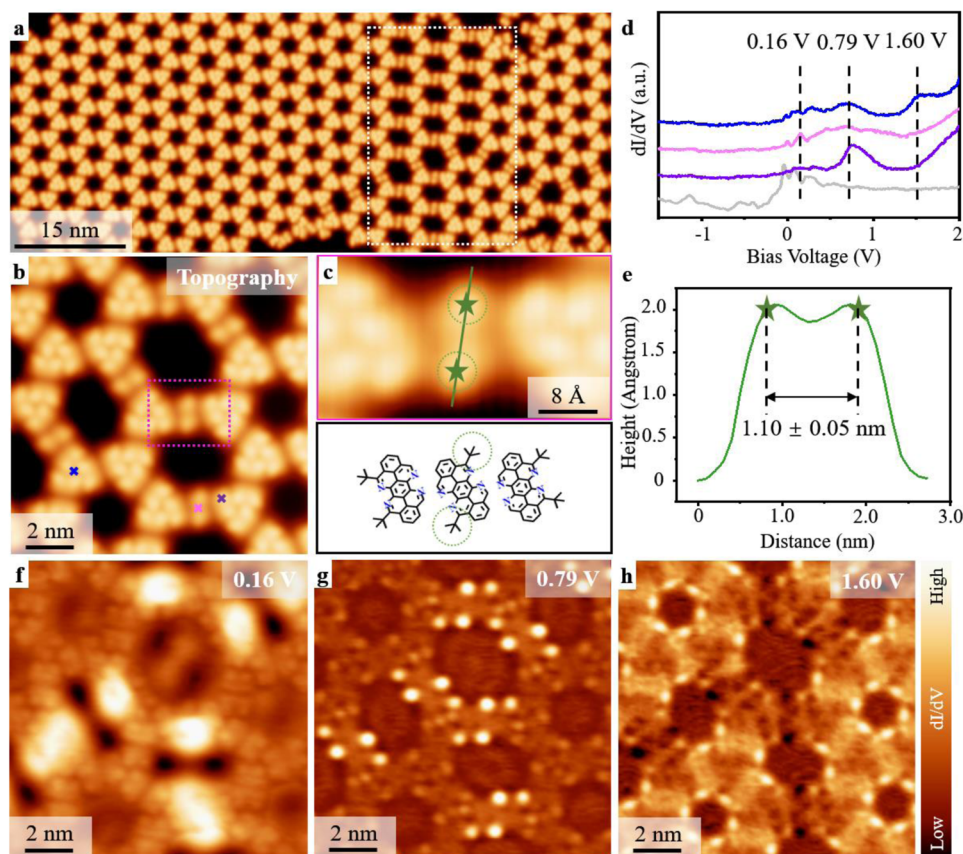


FIG. 3. Formation of 2tBu-TAPP deformed hexagonal networks on Ag(111) after annealing at 488 K for 40 min. (a) STM image of large-area hexagonal networks. (b) Close-up STM image of the doping pore structure. The trimer is marked by a pink dotted square. (c) Magnified images of the pink dotted square in (b) and corresponding molecular models. The green line shows the distance between *tert*-butyl groups in doped 2tBu-TAPP. (d) Differential conductance dI/dV spectra acquired at purple, blue, and pink crosses mentioned in (b). The gray curve is taken on a bare Ag(111) surface. (e) The line profile of the green line in (c). (f)–(h) The corresponding dI/dV maps. Tunneling parameters: (a) $U = -0.60$ V, $I = 0.26$ nA; (b) $U = 0.65$ V, $I = 0.20$ nA; (c) $U = 0.60$ V, $I = 0.40$ nA.

and the individual *tert*-butyl groups of its neighbor 2tBu-TAPP. However, the dI/dV mapping at 1.60 V [Fig. 3(h)] shows that the electronic state density at the doping position is obviously weak.

When the sample was further annealed at 503 K for 40 min, the bent disordered chains were obtained as shown in Fig. 4(a). According to the above analysis, the yellow and green arrows represent the aforementioned 2tBu-TAPP and tBu-TAPP with three *tert*-butyl groups removed, respectively, while the pink arrow represents a rod without any highlights [Fig. 4(b)]. Based on the line profiles shown in Fig. 4(c), we speculate that this is a TAPP molecule with four *tert*-butyl groups removed. To obtain high-quality chains formed by TAPP, the sample was then annealed at 523 K for 40 min. Figures 4(d) and S9(a) show that although the chain structure is still bent and disorderly, the structure of the as-formed chain is basically rod-like TAPP without any bright protrusions. Some representative short chains are characterized by high resolution STM as shown in Figs. 4(e), S9(b), and S9(d). BR-STM in Fig. S9(c) and nc-AFM in Fig. S9(e) indicate that most of the *tert*-butyl removal sites in the TAPP chain structure are passivated by H atoms (as denoted

by the yellow dashed circles in Fig. S9). Meanwhile, metal–organic intermediates stabilized by metal adatoms often facilitate the formation of subsequent C–C covalent products.^{24,25} However, no aligned covalent TAPP chain promoted by C–Ag–C bonds is observed in the experiment. These winding chains may be attributed to multiple metal–organic coordination bonds (C–Ag–C and N–Ag–N bonds), covalent bonds (C–C bonds), and C–H \cdots N hydrogen bonds, which stem from the incomplete saturation of free radicals with a removal of *tert*-butyl groups.

The DFT calculations were conducted to concern the investigation of activation mechanism and potential low-energy barrier pathway for the bond cleavage of C–C(CH₃)₃.²⁶ Similar to recent work in which advanced Au adatoms can effectively reduce the energy barrier for C–Si activation,²⁷ the reaction energy barrier can also further reduce to 1.40 eV with the enhanced activation of C–C via an Ag adatom (Fig. S10). The energetically most favorable energy evolution for the sequential C–C(CH₃)₃ bond activations of 4tBu-TAPP on Ag (111) is shown in Fig. S11. Among them, Ag adatoms are introduced to assist in *tert*-butyl removal (Int1/2/3/4a-b), while

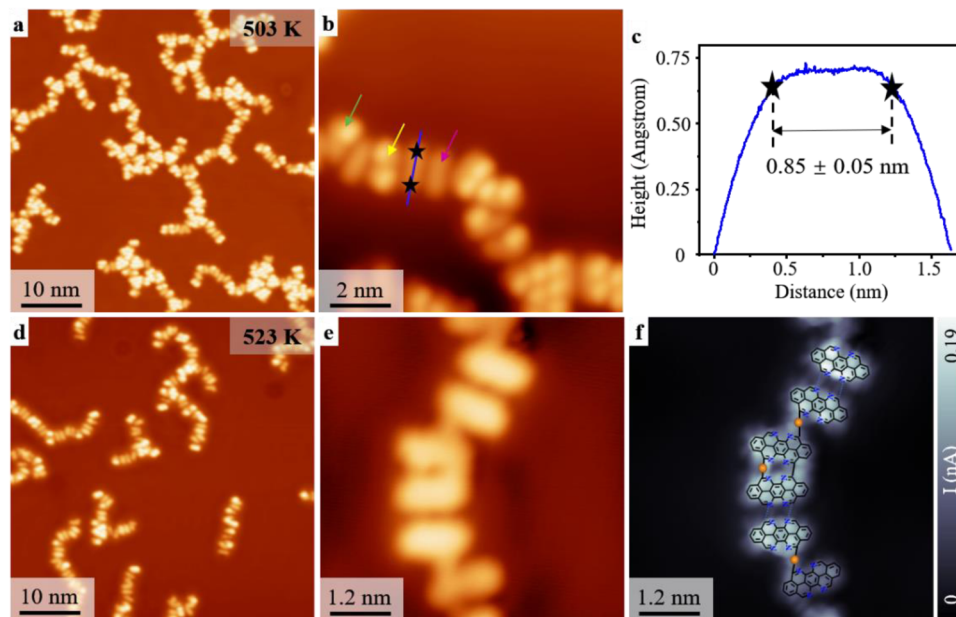


FIG. 4. Formation of TAPP winding chains on Ag(111) after subsequent annealing. (a) Large-scale STM image after annealing at 503 K for 40 min. (b) Close-up STM image of chains. The green, yellow, and pink arrows represent tBu-TAPP, 2tBu-TAPP, and TAPP, respectively. (c) The line profiles of the blue line in (b). (d) Large-scale STM image after annealing at 523 K for 40 min. (e) and (f) High-resolution STM images of a short chain after removing the *tert*-butyl groups completely. Tunneling parameters: (a) $U = -0.80$ V, $I = 0.09$ nA; (b) $U = -0.70$ V, $I = 0.09$ nA; (d) $U = -0.50$ V, $I = 0.06$ nA; (e) $U = -0.20$ V, $I = 0.10$ nA.

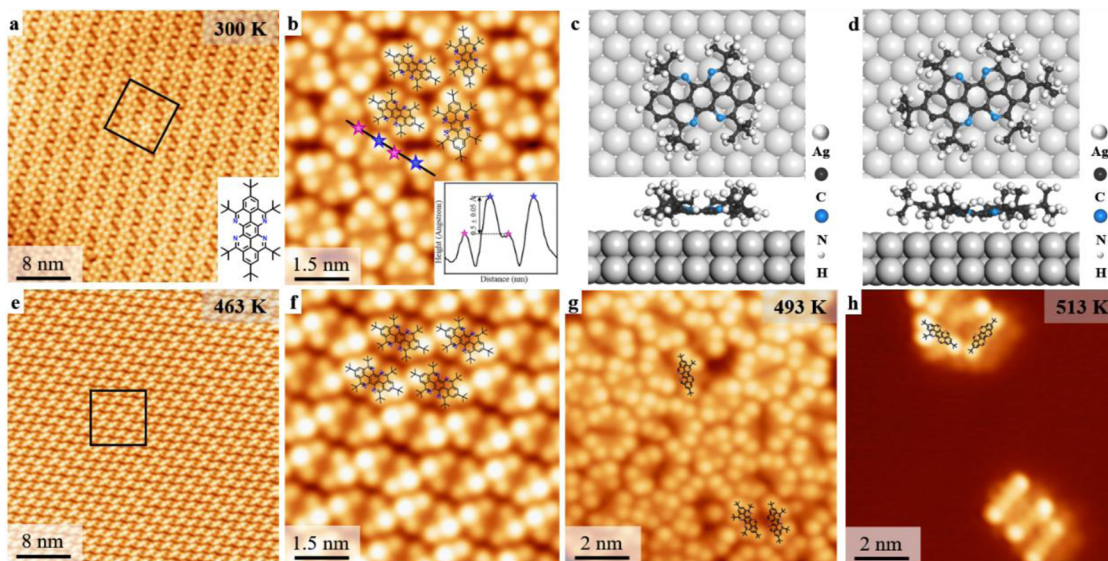


FIG. 5. *Tert*-butyl removal of 6tBu-TAPP on Ag(111) by thermal annealing. (a) Overview STM image of the 6tBu-TAPP molecule deposited at 300 K on the Ag(111) substrate. Inset: chemical structure of 6tBu-TAPP. (b) Zoom-in image of (a). (c) The line profile of the black line in (b). The structural models are covered in the image. The pink and blue stars label the *tert*-butyl group near pyridine nitrogen and at the end, respectively. (d) DFT optimized configuration of 6tBu-TAPP on Ag(111). (e) Overview STM image after annealing at 463 K for 40 min. (f) Zoom-in image of (c). The structural models are covered in the image. STM images after annealing at 493 K (g) and 513 K (h) for 40 min. The structural models are covered in the image. Tunneling parameters: (a) and (e) $U = 0.40$ V, $I = 0.05$ nA; (b) and (f) $U = -0.20$ V, $I = 0.06$ nA; (g) and (h) $U = 0.60$ V, $I = 0.03$ nA.

the final state products result from H saturation (Int1-3 and FS), typically exhibiting lower energies. The complete di-*tert*-butyl progress requires four sequential steps of C–C(CH₃)₃ bond cleavage that converted 4tBu-TAPP into TAPP. It is worth noting that the reaction process is endothermic. Since the extra *tert*-butyl groups are going to get away during the reaction process, the reverse reaction conditions are broken. Therefore, endothermic reactions are possible to happen. The highest energy barrier of C–C(CH₃)₃ bond cleavages is 1.51 eV, suggesting that the di-*tert*-butyl progresses are possible to happen at experimental annealing temperature $T = 503$ K.

We also tried to modulate the assembly structure by controlling the amount of *tert*-butyl group removal through gradient annealing on Au(111) and Cu(111) substrates. However, we only obtained some *tert*-butyl removal products and their cross-coupled structures, which may be due to the different catalytic activities of different substrates (see the details in Figs. S12 and S13).

In order to further investigate the influence of quantities and sites of *tert*-butyl groups on the supramolecular assembly structure, we designed and successfully synthesized the 1,3,6,8,10,13-hexa-*tert*-butyl-4,5,11,12-tetraazaperopyrenes (6tBu-TAPP) precursor. Figures 5(a), 5(b), 5(e), and 5(f) show the regular assembly structure on Ag(111) formed by the van der Waals interaction when annealing at 300 and 463 K, respectively. The close-up image [Figs. 5(b) and 5(f)] depicts that the electronic states of the terminal *tert*-butyl group are brighter than those near pyridine nitrogen, with a height difference of about 0.5 Å [the inset of Fig. 5(b)]. Different from the four *tert*-butyl groups of 4tBu-TAPP possessing the same adsorption height [Fig. 5(c)], the DFT optimized configuration of 6tBu-TAPP explicitly shows that the terminal *tert*-butyl groups are significantly higher [Fig. 5(d)]. Therefore, the four *tert*-butyl groups near pyridine nitrogen first fell off during subsequent annealing. However, the removal amount is not effectively regulated by temperature [Fig. 5(g)]. It may be noted that the introduction of terminal *tert*-butyl group will not only increase the complexity of supramolecular assembly but also increase the adsorption height of molecules and weaken the modulation of surface atoms on the assembly structure. The above speculation can be further verified by the following experiment. When the sample was annealed to 513 K [Fig. 5(h)], with a large number of molecules' desorption, the remaining molecules are almost products with two terminal *tert*-butyl groups. After the removal of four *tert*-butyl groups on the side, the terminal *tert*-butyl groups may increase the adsorption height of the molecule and weaken the surface adsorption.

CONCLUSIONS

Utilizing the 4tBu-TAPP precursor, we have achieved a series of structural transformations from grid-like structures via honeycomb networks to chains on the Ag(111) surface by adjusting the amount of *tert*-butyl group removal through gradient annealing. This structural evolution is directly visualized at an atomic scale using STM. Combined with tip manipulation and DFT calculations, we demonstrate that the honeycomb networks are attributed to N–Ag–N coordination bonds, intermolecular van der Waals interactions, and weak C–H···N hydrogen bonds. In addition, the terminal *tert*-butyl group of 6tBu-TAPP requires a higher removal temperature during annealing on Ag(111) due to its higher adsorption height, which affects the adsorption of molecules and weakens the modulation of

the assembly structure by surface atoms. The finding of our work is helpful for the controllable construction of stable and long-range ordered nanostructures in surface-assisted systems, which can also promote the development of nanostructures in functional molecular devices.

EXPERIMENTAL SECTION

Precursor synthesis

The synthesis route to 3,6,10,13-tetra-*tert*-butyl-4,5,11,12-tetraazaperopyrenes (4tBu-TAPP) and 1,3,6,8,10,13-hexa-*tert*-butyl-4,5,11,12-tetraazaperopyrenes (6tBu-TAPP) is illustrated in Fig. S1, following a previous study.²⁸

Sample preparation and STM measurement

STM experiments were performed with a low-temperature STM from Scienta Omicron operating at a base pressure below 1×10^{-10} mbar. The Ag (111) substrate (MaTeck, 99.999%) was prepared by repeated cycles of Ar⁺ sputtering ($E = 1$ keV) and annealing to 773 K for 30 min. The precursor was synthesized and recrystallized from CH₂Cl₂/acetone, followed by temperature gradient sublimation in ultra-high vacuum. Then, the precursor was thermally deposited onto the clean Ag (111) substrate held at room temperature. All STM images were acquired in the constant-current mode with electron chemically etched tungsten tips at a sample temperature of 4.3 K. The differential conductance spectra and related maps were obtained using a lock-in technique while sweeping the sample bias in an open feedback loop configuration, with a peak-to-peak bias modulation of 5 mV at a frequency of 521 Hz. The STM images were processed by using the software WSxM.²⁹

DFT calculations

Our calculations were carried out using the density functional theory (DFT), the generalized gradient approximation (GGA) for exchange potential³⁰ with the revised Perdew–Burke–Ernzerhof (RPBE) functional,³¹ the projector augmented wave method, and a plane wave basis set as implemented in the Vienna *Ab initio* Simulation Package (VASP).³² Dispersion forces in all calculations were considered at the DFT-D3 correction³³ with a zero-damping variant, which were suggested to be suitable for modeling energetic and structural properties of metal–organic interfaces. The kinetic energy cutoff for the plane wave basis set was set to 450 eV. A $1 \times 1 \times 1$ k-mesh was adopted to sample the first Brillouin zone of the metal–organic interface supercell. A supercell with lattice parameters $a = 19.54$ Å, $b = 20.86$ Å, and $\gamma = 90.62^\circ$ was adopted to describe the 4tBu-TAPP molecule self-assemble lattice in experiment. The adsorption energy was derived from $E_{ads} = E_{total} - 2E_{molecule} - E_{substrate}$, where the energy of substrates contains adatoms. A slab geometry consisting of four layers of Ag atoms was employed to model the Ag (111) surfaces, with the bottom two layers of atoms fixed. In structural relaxation, all atoms except the bottom two layers of Ag were fully relaxed until the net force on every atom was less than 0.02 eV/Å. A supercell with lattice parameters $a = b = 39.05$ Å and $\theta = 120^\circ$ was adopted to describe the 2tBu-TAPP pore structure lattice in experiment. Owing to the high computational cost, the 2tBu-TAPP pore structure model and the

reaction pathway for the di-tert-butyl process of 4tBu-TAPP employ a slab geometry consisting of two layers of Ag atoms to model the Ag (111) surfaces, with the bottom one layer of atoms fixed. In structural relaxation, all atoms except the bottom one layer of Ag were fully relaxed until the net force on every atom was less than 0.02 eV/Å, for the 2tBu-TAPP pore model and the reaction pathway for the di-tert-butyl process of 4tBu-TAPP, respectively. The vacuum layers of models were all larger than 15 Å.

SUPPLEMENTARY MATERIAL

The supplementary material contains detailed descriptions of the precursor synthesis procedures and additional STM and DFT calculation results (PDF).

ACKNOWLEDGMENTS

This work was supported by the National Natural Science Foundation of China (Grant Nos. 62271238, 22372074, and 62301240), Yunnan Fundamental Research Projects (Grant Nos. 202201AT070078, 202101AV070008, 202101AW070010, 202101AU070043, 202201BE070001-009, and 202301AW070017), the Major Basic Research Project of Science and Technology of Yunnan (Grant No. 202302AG050007), Yunnan Innovation Team of Graphene Mechanism Research and Application Industrialization (Grant No. 202305AS350017), Graphene Application and Engineering Research Center of Education Department of Yunnan Providence (Grant No. KKPP202351001), and the Analysis and Testing Foundation of KUST (Grant No. 2021T20170056). Numerical computations were performed at the Hefei Advanced Computing Center.

AUTHOR DECLARATIONS

Conflict of Interest

The authors have no conflicts to disclose.

Author Contributions

Boyu Fu, Yurou Guan, Wei Yuan, Jianqun Geng, and Zhenliang Hao contributed equally to this work.

Boyu Fu: Conceptualization (equal); Data curation (equal); Investigation (equal); Methodology (equal); Visualization (equal); Writing – original draft (equal). **Yurou Guan:** Data curation (equal); Formal analysis (equal). **Wei Yuan:** Formal analysis (equal);

Writing – review & editing (equal). **Jianqun Geng:** Data curation (equal); Methodology (equal). **Zhenliang Hao:** Data curation (equal). **Zilin Ruan:** Formal analysis (equal). **Shijie Sun:** Formal analysis (equal). **Yong Zhang:** Formal analysis (equal). **Wei Xiong:** Formal analysis (equal). **Lei Gao:** Conceptualization (equal); Supervision (equal). **Yulan Chen:** Supervision (equal). **Wei Ji:** Conceptualization (equal); Supervision (equal). **Jianchen Lu:** Conceptualization (equal); Formal analysis (equal); Supervision (equal); Writing – review & editing (equal). **Jinming Cai:** Funding acquisition (equal); Supervision (equal).

DATA AVAILABILITY

The data that support the findings of this study are available within the article and its supplementary material.

REFERENCES

- 1 J. V. Barth, G. Costantini, and K. Kern, *Nature* **437**, 671 (2005).
- 2 L. Bartels, *Nat. Chem.* **2**, 87 (2010).
- 3 R. Otero *et al.*, *Adv. Mater.* **23**, 5148 (2011).
- 4 Y. Ke *et al.*, *Science* **319**, 180 (2008).
- 5 C. J. Baddeley *et al.*, *Top. Catal.* **54**, 1348 (2011).
- 6 S. Lei *et al.*, *ChemComm* **2008**, 703.
- 7 L. Gross *et al.*, *Phys. Rev. B* **71**, 165428 (2005).
- 8 K. Tahara *et al.*, *J. Am. Chem. Soc.* **128**, 16613 (2006).
- 9 W. Xu *et al.*, *Small* **4**, 1620 (2008).
- 10 F. Cheng *et al.*, *Nat. Commun.* **9**, 4871 (2018).
- 11 J. Lawrence *et al.*, *Nat. Commun.* **11**, 2103 (2020).
- 12 U. S. Jeon *et al.*, *Appl. Surf. Sci.* **432**, 332 (2018).
- 13 J. Lu *et al.*, *J. Phys. Chem. Lett.* **8**, 326 (2017).
- 14 S. A. Saleh and H. I. Tashtoush, *Tetrahedron* **54**, 14157 (1998).
- 15 L. Wang and D. L. J. Clive, *Org. Lett.* **13**, 1734 (2011).
- 16 Q. Tan *et al.*, *J. Phys. Chem. C* **119**, 8155 (2015).
- 17 K. Sheng *et al.*, *J. Phys. Chem. C* **118**, 3088 (2014).
- 18 Q. Sun *et al.*, *Appl. Phys. Lett.* **103**, 013103 (2013).
- 19 K. H. Au Yeung *et al.*, *J. Phys. Chem. Lett.* **11**, 6892 (2020).
- 20 S. Mahapatra *et al.*, *J. Am. Chem. Soc.* **144**, 2051 (2022).
- 21 J. Cho *et al.*, *J. Chem. Phys.* **133**, 234707 (2010).
- 22 X. Zhang *et al.*, *ACS Nano* **13**, 1385 (2019).
- 23 X. Liu *et al.*, *Angew. Chem., Int. Ed.* **61**, e202112798 (2022).
- 24 R. Pawlak *et al.*, *Angew. Chem., Int. Ed.* **60**, 8370 (2021).
- 25 R. Pawlak *et al.*, *J. Am. Chem. Soc.* **142**, 12568 (2020).
- 26 W. Gao *et al.*, *ACS Nano* **16**, 6578 (2022).
- 27 K. Ma *et al.*, *J. Am. Chem. Soc.* **144**, 8789 (2022).
- 28 W. Yuan *et al.*, *Angew. Chem., Int. Ed.* **59**, 9940 (2020).
- 29 I. Horcas *et al.*, *Rev. Sci. Instrum.* **78**, 013705 (2007).
- 30 J. Klimeš, D. R. Bowler, and A. Michaelides, *Phys. Rev. B* **83**, 195131 (2011).
- 31 B. Hammer, L. B. Hansen, and J. K. Nørskov, *Phys. Rev. B* **59**, 7413 (1999).
- 32 G. Kresse and J. Furthmüller, *Phys. Rev. B* **54**, 11169 (1996).
- 33 S. Grimme *et al.*, *J. Chem. Phys.* **132**, 154104 (2010).